Chinese Chemical Letters 37 (2026) 111339

Contents lists available at ScienceDirect

Chinese Chemical Letters

journal homepage: www.elsevier.com/locate/cclet

# An injectable hydrogel for chemodynamic therapy-induced ferroptosis in malignant melanoma

Yongzhi Wu[a,b,1], Rong He[a,b,1], Bowen Tan[a], Longjiang Li[b,*], Jinfeng Liao[a,*]

[a] State Key Laboratory of Oral Diseases & National Center for Stomatology & National Clinical Research Center for Oral Diseases, West China Hospital of Stomatology, Sichuan University, Chengdu 610041, China
[b] State Key Laboratory of Oral Diseases & National Center for Stomatology & National Clinical Research Center for Oral Diseases & Department of Head and Neck Oncology, West China Hospital of Stomatology, Sichuan University, Chengdu 610041, China

ARTICLE INFO

*Article history:*
Received 11 March 2025
Revised 15 May 2025
Accepted 16 May 2025
Available online 16 May 2025

*Keywords:*
Chemodynamic therapy
Cupric peroxide nanoparticles
Hydrogel
pH-responsive
Ferroptosis

ABSTRACT

Chemodynamic therapy (CDT) represents a novel strategy for the safe treatment of malignant melanoma. It capitalizes on transition metal-catalyzed Fenton-like reactions to generate hydroxyl radicals (•OH) that directly eradicate tumor cells. However, its efficacy is hindered in the tumor microenvironment (TME) by low endogenous hydrogen peroxide ($H_2O_2$) levels and high glutathione (GSH) content. To overcome these limitations, an injectable self-healing adipic dihydrazide (ADH)-modified hyaluronic acid (HA) (HA-ADH)/aldehyde terminated polyethylene glycol (PEG-CHO)/PVP-cupric peroxide ($CuO_2$) nanoparticles (HPC) hydrogel was developed. This hydrogel system is injectable, pH-responsive, self-healing, and enables sustained GSH depletion through dual $Cu^{2+}$/•OH-mediated mechanisms. The HPC hydrogel system not only compensates for the TME's endogenous $H_2O_2$ deficiency through self-generated $H_2O_2$ but also disrupts redox homeostasis *via* GSH oxidation, thereby inactivating glutathione peroxidase 4 (GPX4) and promoting lipid peroxide accumulation to trigger ferroptosis in melanoma cells. Such a strategy represents a promising approach to achieve enhanced CDT and potent ferroptosis induction by synergizing dual GSH-depleting cycling and self-sufficient $H_2O_2$ generation.

© 2025 Published by Elsevier B.V. on behalf of Chinese Chemical Society and Institute of Materia Medica, Chinese Academy of Medical Sciences.

Malignant melanoma remains the most life-threatening form of cutaneous malignancy, associated with high invasiveness and early metastasis. Current management strategies encompass surgical resection for localized disease, alongside systemic therapies such as BRAF/MEK inhibitors and PD-1/PD-L1 checkpoint blockade to address advanced cases [1–3]. Despite these approaches, acquired resistance substantially limits long-term survival outcomes, particularly in metastatic patients, resulting in a poor 5-year prognosis [4,5]. To address this critical issue, many potent therapeutic modalities such as photothermal therapy (PTT) [6,7], chemodynamic therapy (CDT) [8,9], sonodynamic therapy (SDT) [10], photodynamic therapy (PDT) [11], photoacoustic therapy (PAT) [12], magnetic hyperthermia (MHT) [13] and high-intensity focused ultrasound (HIFU) [14] have been developed to surmount traditional treatment limitations in melanoma management.

CDT emerges as an attractive modality due to its self-sustaining reactive oxygen species (ROS) generation mechanism (which obviates the need for additional external stimuli), cost-effectiveness, and non-specific cytotoxicity [15,16]. The therapeutic principle relies on transition metal ions (*e.g.*, $Fe^{2+}$, $Cu^{+}$, $Mn^{2+}$) catalyzing the Fenton-like reaction in the tumor microenvironment (TME), where hydrogen peroxide ($H_2O_2$) is decomposed into highly reactive hydroxyl radicals (•OH) to kill cancer cells directly [17–19]. However, the inherent limitation lies in the insufficient endogenous $H_2O_2$ concentration ($\sim 100 \times 10^{-6}$ mol/L) within the TME to sustain effective •OH production for therapeutic outcomes [8]. Nanomaterials designed to enhance intracellular $H_2O_2$ generation have emerged as a promising avenue. Notably, acid-responsive metal peroxides (*e.g.*, $CaO_2$, $CuO_2$, $BaO_2$, $MgO_2$) have garnered attention as innovative candidates. Their pH-triggered decomposition at acidic pH ($\sim$6.0) within the TME enables selective $H_2O_2$ release while minimizing systemic exposure [20,21].

The elevated glutathione (GSH) levels (up to 1000-fold higher than normal tissues) in malignant cells create a robust antioxidant defense network that significantly compromises CDT efficacy through •OH scavenging [22]. This intrinsic redox imbalance creates a therapeutic resistance barrier, as evidenced by the compromised ROS generation capacity during CDT. Conversely, transition metal ions (*e.g.*, $Cu^{2+}$) serve as catalytic redox mediators that disrupt this defense system by oxidizing GSH, thereby creating a GSH-

* Corresponding authors.
*E-mail addresses:* liscu1992@163.com (L. Li), liaojinfeng.762@163.com (J. Liao).
[1] These authors contributed equally to this work.

https://doi.org/10.1016/j.cclet.2025.111339
1001-8417/© 2025 Published by Elsevier B.V. on behalf of Chinese Chemical Society and Institute of Materia Medica, Chinese Academy of Medical Sciences.

deficient TME that synergistically enhances CDT outcomes through the inhibition of ROS detoxification [23]. Continuous GSH depletion triggers glutathione peroxidase 4 (GPX4) inactivation, a pivotal event that compromises the lipid peroxide repair machinery and activates ferroptosis [24]. Ferroptosis, a distinctive programmed cell death mechanism, is driven by iron-catalyzed lipid peroxidation, ultimately leading to catastrophic membrane destabilization. Extensive research highlights its therapeutic potential, particularly as a targeted strategy for refractory cancers that exhibit resistance to conventional treatments [25]. In certain circumstances, ferroptosis and CDT could be intricately linked. High GSH levels in malignant cells impede CDT-induced ROS production. Thus, triggering ferroptosis can boost ROS generation. Conversely, CDT can also induce the lipid-peroxide-mediated cell death process of ferroptosis, enabling the two to surmount the shortcomings of single-modality treatments and augment anti-cancer therapeutic efficacy. However, conventional CDT administration modalities, such as oral and intravenous routes, are often associated with significant off-target toxicity due to non-specific biodistribution. Even local CDT application faces limitations from rapid drug release and high-concentration-mediated cytotoxicity, which restricts its clinical utility.

In recent years, injectable hydrogels have emerged as promising functional agents/drug delivery platforms owing to their rapid sol-gel transitions enabled by dynamic covalent bonds, including Schiff base cross-linking [26], borate-diol interactions [27], and Diels-Alder reactions [28]. These mechanisms not only facilitate controlled drug release but also enhance spatiotemporal specificity, overcoming the limitations of conventional systemic therapies [29,30]. Notably, Schiff-based hydrogels exhibit pH-responsive drug release behavior: They degrade and swell efficiently in the acidic TME while maintaining structural integrity at physiological pH, thereby minimizing premature drug leakage and ensuring targeted therapy [31].

Herein, we propose a GSH-depleting strategy utilizing adipic dihydrazide (ADH)-modified HA (HA-ADH)/aldehyde terminated polyethylene glycol (PEG-CHO) (HP) to deliver pH-responsive cupric peroxide ($CuO_2$) nanoparticles into the TME of melanoma cells. This self-healing hydrogel system (HPC) exhibits acid-triggered kinetics and maintains structural integrity under complex mechanical stress, enabling sustained GSH depletion to induce ferroptosis. Notably, the HPC hydrogel system self-supplies $H_2O_2$ through its redox-active components, compensating for the inherent $H_2O_2$ deficiency within the TME of melanoma cells. The integration of injectable hydrogels with functional $CuO_2$ nanoparticles addressed the limitations of conventional CDT. Both *in vitro* and *in vivo* results demonstrated HPC's potent capabilities in eradicating malignant melanoma cells and inhibiting distant metastasis. Therefore, this study offers novel insights for the development of highly efficient and safe melanoma therapy.

The $CuO_2$ nanoparticles were synthesized as shown in Fig. 1A. By sequentially adding PVP, $CuSO_4$, NaOH, and $H_2O_2$, the dispersion color gradually transitioned from light blue to green and subsequently to yellow, indicating successful $CuO_2$ nanoparticles formation. The ultraviolet (UV) spectrophotometric analysis was conducted to characterize the synthesis process of $CuO_2$ nanoparticles (Fig. 1B). The appearance of a new absorption band at 400–600 nm indicated the successful preparation of $CuO_2$ nanoparticles [32]. The atomic force microscopy (AFM) image demonstrated that the size of $CuO_2$ nanoparticles was homogeneous with a thickness of about 96.80 nm (Fig. 1C and Fig. S1 in Supporting information).

In addition, $KMnO_4$ was utilized to confirm the successful synthesis of $CuO_2$ nanoparticles. Upon acidification, $CuO_2$ nanoparticles decomposed to release $Cu^{2+}$ and $H_2O_2$. Subsequently, $KMnO_4$ reacted with $H_2O_2$ to generate yellow $Mn^{2+}$ (Fig. 1D). And the UV absorption spectrum exhibited distinct changes after $KMnO_4$ treatment (Fig. 1E). The particle size of $CuO_2$ nanoparticles was quantitatively analyzed by dynamic light scattering (DLS), revealing an average diameter of 121.84 nm and a low polydispersity index (PDI) of 0.062. This low PDI indicates a narrow size distribution and favorable colloidal stability (Fig. 1F). The result is consistent with the AFM detection.

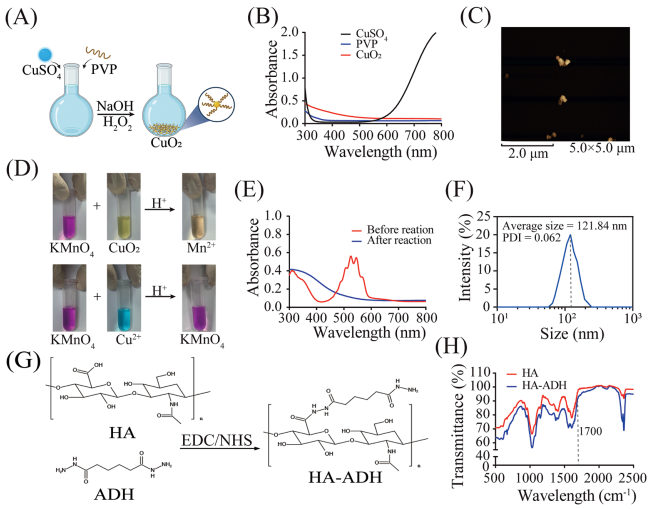



**Fig. 1.** Synthesis and characterization analysis of $CuO_2$ nanoparticles and HA-ADH composites. (A) The schematic illustration of the preparation of $CuO_2$ nanoparticles. (B, C) The UV absorption spectrum and the AFM image of $CuO_2$ nanoparticles. (D, E) The macroscopic observation and UV absorption spectrum of the reaction between $KMnO_4$ and $CuO_2$ nanoparticles under acidic conditions. (F) The particle size of $CuO_2$ nanoparticles. (G) The preparation process of HA-ADH. (H) FTIR spectroscopy comparison between HA and HA-ADH. Fig. 1A was created with BioRender.com.

The proton nuclear magnetic resonance ($^1$H NMR) spectrum and Fourier-transform infrared (FTIR) spectrum were employed to detect the preparation of HA-ADH (Figs. 1G and H, Fig. S2 in Supporting information). HA-ADH showed a new characteristic absorption peak at 1700 $cm^{-1}$ compared to HA, which demonstrated the successful introduction of ADH groups. The emerging peak at 1.65 and 2.39 ppm in the $^1$H NMR spectrum indicates the successful preparation of HA-ADH (Fig. S2). The grafting rate of HA-ADH was about 34.5 %. Importantly, the successful modification of HA with ADH provides a functionalized backbone for the hydrogel system. A grafting rate of 34.5 % can potentially optimize the hydrogel's cross-linking density and responsiveness.

Next, we explored the functional properties of $CuO_2$ nanoparticles that were central to the CDT mechanism, specifically for its ·OH-generating and GSH-depleting capabilities. ·OH can be generated through a Fenton-like reaction, primarily mediated by low-valence metal ions (*e.g.*, $Fe^{2+}$ and $Cu^{+}$) reacting with $H_2O_2$ [33]. In the case of $CuO_2$ nanoparticles, acidity induces $Cu^{2+}$ release. Typically, TME contains abundant GSH, which can reduce high-valence metal ions (such as $Fe^{3+}$/$Cu^{2+}$) to generate Fenton reagents like $Fe^{2+}$/$Cu^{+}$ [34]. 3,3′,5,5′-Tetramethylbenzidine (TMB) undergoes oxidation by ·OH, resulting in a blue color change, and is thus widely used for ·OH detection. The mechanism of TMB color development involves electron loss in the benzidine structure, leading to dimer charge-transfer complex formation (Fig. 2A). As shown in Figs. 2B and C, $Cu^{2+}$ would catalyze $H_2O_2$ decomposition into ·OH under GSH presence, producing a characteristic absorption peak at 655 nm and inducing a distinct blue color shift in solution. Critically, $CuO_2$ nanoparticles exhibited exceptional ·OH-generating capacity under acidic conditions. The kinetics of ·OH production by $CuO_2$ nanoparticles were investigated through systematic optimization of reaction time and pH, with ·OH levels quantified as shown in Figs. 2D and E. These results confirmed the sustained and pH-responsive ·OH production of $CuO_2$ nanoparticles over time.

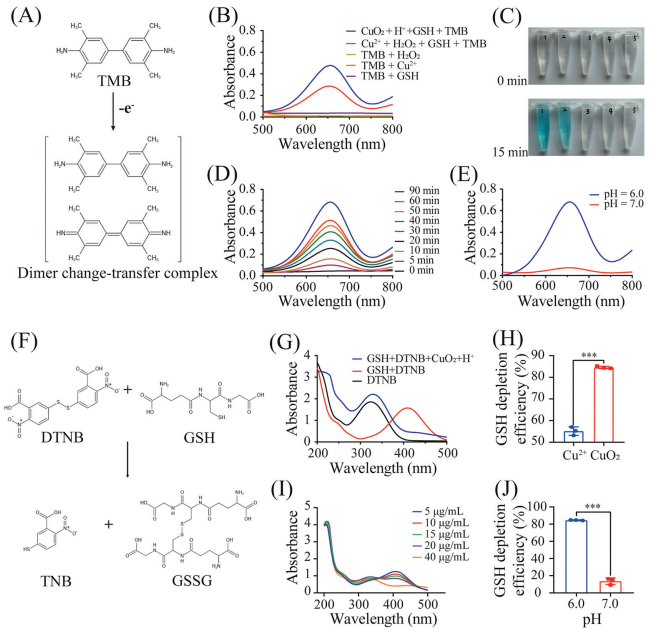



**Fig. 2.** ˙OH-generation and GSH-depleting properties of $CuO_2$ nanoparticles. (A) The mechanism of blue coloration of TMB after reaction with ˙OH. (B) UV absorption profiles and the corresponding (C) macroscopic images of TMB-reacted components. The EP tubes labeled 1–5 correspond to the reactions of $CuO_2 + H^+ + GSH + TMB$, $Cu^{2+} + H_2O_2 + GSH + TMB$, $TMB + H_2O_2$, $TMB + Cu^{2+}$, and $TMB + GSH$, respectively. (D) The kinetic UV absorption profiles of $CuO_2$ nanoparticles reacting with TMB in the acid buffer. (E) Acid-dependent UV–vis absorption characteristics of $CuO_2$-TMB interactions. (F) Chemical structure of DTNB-GSH reaction mechanism. (G) Spectroscopic analysis of DTNB-reacted components. (H) Comparative GSH consumption of $Cu^{2+}$ and $CuO_2$ nanoparticles. (I) Dose-dependent GSH depletion kinetics monitored by UV absorption. (J) pH-dependent GSH-depleting efficiency of $CuO_2$ nanoparticles. Data are presented as mean ± standard deviation (SD) ($n = 3$). $^{***}P < 0.001$.

The efficient ˙OH generation by $CuO_2$ nanoparticles under TME-mimicking environmental conditions (pH 6.0) is highly promising for enhancing CDT during anti-tumor treatments. Furthermore, the continuous production of ˙OH over time may cause cumulative damage to tumor cells.

Next, the GSH scavenging capacity of $CuO_2$ nanoparticles was evaluated using the DTNB-based method. In this method, DTNB reacted with the sulfhydryl groups of GSH to produce yellow 2-nitro-5-thiobenzoic acid (TNB) (Fig. S3 in Supporting information), which exhibited a characteristic absorption peak at 412 nm, while unreacted DTNB showed negligible absorbance above 400 nm (Figs. 2F and G). A standard curve for GSH consumption was established based on absorbance measurements at 412 nm (Fig. S4 in Supporting information) Subsequently, the quantitative GSH scavenging efficiency of $CuO_2$ nanoparticles was determined. Notably, $CuO_2$ nanoparticles exhibited approximately 34.8 % higher GSH scavenging efficiency compared to $Cu^{2+}$ (Fig. 2H). Moreover, this capacity is enhanced continuously with increasing $CuO_2$ nanoparticle concentrations (Fig. 2I), which may be attributed to the cyclic regeneration of $Cu^{2+}$ *via* the following mechanism: $Cu^{2+}$ consumes GSH to generate $Cu^+$, which then catalyzes $H_2O_2$ decomposition to regenerate $Cu^{2+}$. Interestingly, under physiological pH conditions, $CuO_2$ nanoparticles exhibited negligible GSH scavenging activity. However, this effect was significantly amplified upon exposure to an acidic environment (Fig. 2J). The superior GSH scavenging efficiency of $CuO_2$ nanoparticles, along with its pH-dependent activation, is in line with the concept of disrupting the tumor cells' antioxidant defense system. Therefore, the functional nanoparticles could provide a TME-targeted approach to enhancing CDT efficacy in the acidic TME.

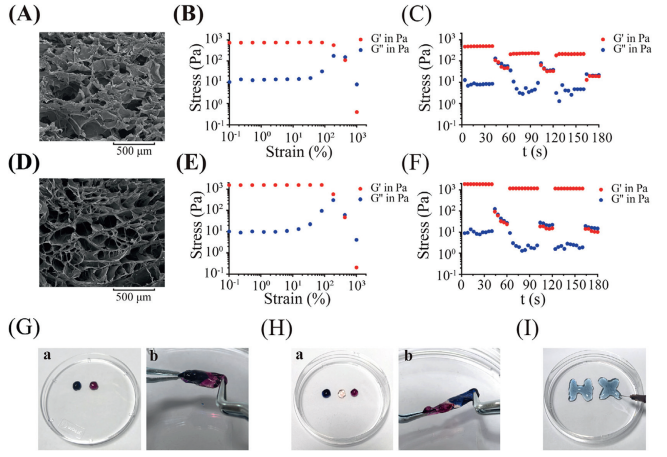



**Fig. 3.** Physicochemical properties of HP and HPC hydrogels. (A) Cross-sectional microstructure analysis, (B, C) shear deformation behavior evaluation, and self-healing performance under continuous strain testing of HP hydrogel. (D) Cross-sectional morphological characterization, (E, F) corresponding shear strain measurements, self-repairability assessment under analogous cyclic loading conditions of HPC hydrogel. (G, H) Self-healing properties tests of HP and HPC hydrogels after labeling with alizarin red/methylene blue (a, pre-fusion state; b, stretching after fusion). (I) Sequential writing demonstration of "HX" characters using a syringe-injected HPC hydrogel.

Motivated by the unique ˙OH-generating and GSH-depleting capabilities of $CuO_2$ nanoparticles, comprehensive characterization experiments were subsequently conducted on the synthesized hydrogel carrier systems. The features revealed by SEM-mapping and energy dispersive spectrometry (EDS) analyses further validated the successful preparation of the HPC hydrogel (Fig. S5 in Supporting information). The SEM images (Figs. S5 and S6 in Supporting information) clearly demonstrate that $CuO_2$ nanoparticles are uniformly dispersed within the hydrogel matrix. The HPC hydrogel could well maintain the morphological structure of the encapsulated nanoparticles without further aggregation. This anti-aggregation property facilitates homogeneous nanoparticle distribution, which is essential for achieving reliable anti-tumor treatment. Previous studies have established that the integration of nanomaterials within hydrogel systems can enhance their mechanical properties [35]. Herein, HP hydrogel without $CuO_2$ nanoparticles was prepared as the control. As shown in Figs. 3A and D, both HP and HPC hydrogels exhibited three-dimensional network structures. The mechanical property of the hydrogels was improved upon $CuO_2$ nanoparticles integration (Fig. S7 in Supporting information). At shear strains exceeding 200 %, the storage modulus of both HP and HPP hydrogels still outstripped their loss modulus, indicating the good preservation of their gel state (Figs. 3B and E). The capacity of HPC hydrogel to preserve its gel state under high-shear strains is crucial for its *in vivo* stability. Such an outstanding ability allows them to endure the intricate and dynamic mechanical forces within the complex physiological environment of the body.

The self-healing behavior of hydrogels was assessed through rheological and dye staining techniques. The hydrogels were subjected to alternating low (1 %) and high (500 %) shear strains. After three complete gel-sol transitions, the storage and loss moduli of HPC hydrogel remained stable compared to HP hydrogel (Figs. 3C and F). Furthermore, the dyed hydrogels exhibited reversible stretchability after fusion (Figs. 3G and H). The self-healing property of HPC hydrogel is highly promising for biomedical applications. In complex physiological and pathological settings, tissues face diverse mechanical stresses like stretching, compression, and torsion. Our self-healing hydrogel system could maintain structural integrity, repair mechanical damage, and ensure continuous release

of therapeutic agents during *in vivo* anti-tumor therapies. We further studied the release profile of $CuO_2$ nanoparticles from HPC under different pH conditions. As showed in Fig. S8 (Supporting information), the cumulative release reached 71.4 % at pH 6 within 24 h (compared to 30.3 % at pH 7), with almost complete release of $CuO_2$ nanoparticles observed at 72 h at pH 6. This confirms the sustained and pH-dependent release behavior of $CuO_2$ nanoparticles from HPC, which is consistent with the pH-responsive mechanism observed in similar systems [36]. Such pH-responsive $CuO_2$ nanoparticle release kinetics, together with the TME-triggered $^{\bullet}OH$ production (as demonstrated in Fig. 2E) establish a promising application of the selective anti-tumor treatment with minimized systemic toxicity.

Notably, the synthesized HPC hydrogel exhibits outstanding injectability. HPC hydrogel samples loaded into a syringe could be injected smoothly for writing applications, and the extruded gel retained its structural integrity (Fig. 3I). The mechanical properties of HPC hydrogel are specifically engineered to balance appropriate mechanical performance while maintaining excellent injectability, allowing for minimally invasive needle delivery. After *in vivo* injection, the self-healing ability of the hydrogel system helps restore its structural integrity and forming a stable *in situ* depot around tumors. This depot ensures controlled release of therapeutic agents into the TME while maintaining spatial stability to prevent off-target distribution. Notably, the incorporation of functional nanoparticles enhances the *in vivo* stability of the hydrogel system, thereby supporting sustained antitumor activity (Fig. S9 in Supporting information).

We further evaluate the biocompatibility of the hydrogels and their impact on tumor cells, which directly relates to the therapeutic potential of the HPC hydrogel system. To evaluate the cellular biocompatibility of HP hydrogel, we assessed the effects of HP hydrogel leachate on NIH-3T3 and B16 cell proliferation under neutral pH condition. As shown in Fig. S10 (Supporting information), when cultured in DMEM/RPMI 1640 medium containing different concentrations of HP hydrogel leachates, no significant differences in cell growth kinetics were observed among all experimental groups (Figs. S10A and D). These results collectively demonstrate that HP hydrogel exhibited excellent biocompatibility, suggesting minimal cytotoxicity and potential safety for normal tissues under physiological pH environments.

TME is characterized by acidic pH and high GSH levels, which may reduce CDT efficiency. Within this context, the glutathione/glutathione disulfide (GSH/GSSG) redox system plays a critical role in scavenging $^{\bullet}OH$ and alleviating oxidative stress. After co-culture with free $CuO_2$ nanoparticles and HPC hydrogel, B16 cells exhibited a significant decline in GSH content (Fig. S10B). The GSH/GSSG ratio, reflecting intracellular redox homeostasis, was notably decreased in tumor cells due to elevated oxidative stress (Fig. S10C) [37]**.** This ratio was further reduced upon free $CuO_2$ nanoparticles or HPC hydrogel treatment, indicating that CDT disrupts redox balance in B16 cells and enhances $^{\bullet}OH$-mediated tumor-killing effects. Therefore, the significant reduction in GSH content and the GSH/GSSG ratio validates the disruption of the tumor cells' antioxidant defense system.

Results of the cell counting kit-8 (CCK-8) and live-dead assays demonstrated that both free $CuO_2$ and HPC hydrogel induced marked tumor cell death, with a positive correlation between red fluorescence intensity (indicative of dead cells) and cell death proportion observed in these groups (Figs. S10E and F). Notably, the free $CuO_2$ group exhibited significantly higher cytotoxic effects compared to the HPC group, suggesting that $CuO_2$ nanoparticles may act as a critical factor in augmenting CDT-induced toxicity *in vitro*.

Next, we delve deeper into the underlying mechanism of how the CDT system in the HPC hydrogel elicits anti-tumor effects, specifically through ROS generation and ferroptosis induction. This ferroptosis-mediated process is a crucial element of our proposed therapeutic strategy. To investigate the ferroptosis induction capacity of the CDT system, B16 cells were treated with different treatment modalities (control, HP, free $CuO_2$ or HPC) for 6 h. 2′,7′-Dichlorodihydrofluorescein diacetate (DCFH-DA) staining confirmed that $CuO_2$ nanoparticles significantly elevated intracellular ROS levels in B16 cells. As shown in Fig. S11 (Supporting information), due to the direct absorption by tumor cells, the free $CuO_2$ group exhibited significantly higher ROS production compared to the HPC group (Fig. S11A). Further aminophenyl fluorescein (APF) detection verified that the generated ROS was $^{\bullet}OH$ (Fig. S11B). Subsequently, ferroptosis-related parameters including lipid peroxidation levels and GPX4 expression were evaluated *via* Liperfluo staining and Western blot analysis. Notably, comparative fluorescence analysis demonstrated that both free $CuO_2$ and HPC formulations generated substantially stronger green fluorescence signals compared to control groups, with free $CuO_2$ showing greater intensity than HPC (Fig. S11C). Western blot analysis consistently revealed a significant downregulation of GPX4 expression in both the free $CuO_2$ group and the HPC group. Remarkably, free $CuO_2$ nanoparticles induced a more substantial suppression of GPX4 expression than the HPC hydrogel did (Fig. S11D). These findings collectively indicate enhanced lipid peroxidation in both free $CuO_2$ and HPC groups. The notable rise in intracellular ROS levels, lipid peroxidation, and downregulation of GPX4 are hallmarks of intracellular $^{\bullet}OH$ generation and ferroptosis induction. These results establish that HPC hydrogel triggers ferroptosis in B16 cells through redox dysregulation mechanisms. Importantly, HPC hydrogel exhibited attenuated lipid peroxidation levels compared to direct drug administration, indicating a more controlled and safer means of inducing ferroptosis by preventing excessive oxidative stress and off-target effects.

Inspired by the comprehensive characterizations, *in vitro* investigations, and elucidated mechanisms of ferroptosis-mediated antitumor effects, we were motivated to pursue *in vivo* studies, which were approved by the Animal Ethics Committee of the State Key Laboratory of Oral Diseases, West China Hospital of Stomatology, Sichuan University. To investigate the antitumor efficacy of CDT under clinically relevant conditions, a B16 tumor-bearing mouse model was established. Mice were respectively treated with 100 μL saline, HP hydrogel, free $CuO_2$, or HPC hydrogel to evaluate their treatment responses (Fig. 4A). The results of comparative photography revealed that the HPC group exhibited superior tumor growth inhibition compared to other groups after 10 days of treatment (Fig. 4B). This visual trend was corroborated by quantitative analysis of tumor volume and weight (Figs. 4C and D), where the HPC group displayed the smallest tumor volume at the experimental endpoint. Histopathological evaluation *via* hematoxylin and eosin (HE) staining demonstrated that $CuO_2$- and HPC-treated tumors exhibited significantly larger necrotic areas compared to the Control and HP groups. Furthermore, immunohistochemical (IHC) analysis of tumor tissues confirmed that the treatment of both $CuO_2$ nanoparticles and HPC hydrogel induced marked downregulation of GPX4 expression in B16 cells (Fig. 4E). Previous studies have shown that copper nanoparticles exhibit long-term stability under physiological conditions and are primarily metabolized and cleared through hepatic and renal pathways [38,39]. It was reported that excessive systemic administration might be associated with hepatic, renal, neuronal, and immunological toxicity in animal models [40–42]. However, our localized delivery strategy employed a significantly lower dose, which is under the previously reported safe dose [42]. To comprehensively evaluate the local and systemic biocompatibility of $CuO_2$ nanoparticles within the HPC hydrogel system, we performed subcutaneous injections in mice and collected skin tissue samples on days 3, 5, 7, and 10 post-injection for histological analysis (Fig. S12 in Supporting

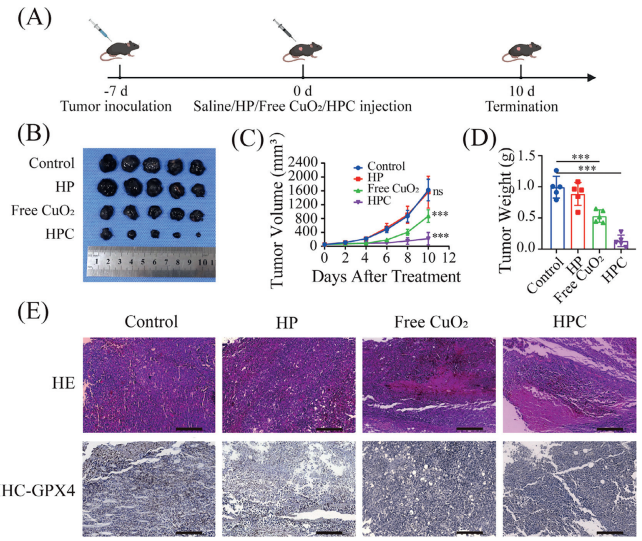



**Fig. 4.** Therapeutic outcomes and molecular characterization in tumor-bearing models. (A) Therapeutic regimen timeline for orthotopic tumor models (B) Macroscopic visualization of excised tumors across experimental cohorts on day 10. (C) Volumetric analysis of neoplastic tissues. (D) Gravimetric quantification of tumor burden. (E) Histopathological assessment of necrotic areas *via* HE staining, and molecular profiling of GPX4 expression through IHC staining (scale bar: 200 μm). Data are presented as mean ± SD ($n = 5$). $^{***}P < 0.001$. ns, not significant. Fig. 4A was created with BioRender.com.

information). HE staining revealed no signs of inflammation or tissue damage in the surrounding skin, indicating favorable local tolerance. Furthermore, systemic toxicity was assessed by HE staining of major organs, including the heart, liver, spleen, lungs, and kidneys, with no significant histopathological abnormalities observed across all treatment groups (Fig. S13 in Supporting information). Throughout the 10-day observation period, no signs of systemic toxicity or abnormal behaviors were detected, further confirming the excellent biocompatibility of the HPC hydrogel. Further histopathological evaluation revealed distinct metastatic lesions in pulmonary and renal tissues of the Control and HP groups, with scattered metastatic cells detected in the free $CuO_2$ group. However, no significant metastatic lesions were detected in the HPC group, confirming the potent anti-metastatic efficacy of HPC hydrogel against B16 melanoma progression (Fig. S13). These results demonstrate that $CuO_2$ nanoparticles exhibit potent antitumor activity. Once encapsulated within the HP hydrogel system, $CuO_2$ nanoparticles give rise to a sustained tumor-killing profile. This inherent property enables $CuO_2$ nanoparticles to continuously exert tumor-suppression effects on tumors over a 10-day treatment regimen. Consequently, the HPC hydrogel system not only elicits potent tumor-killing effects but also effectively impedes potential distant metastasis. We further evaluated the *in vitro* and *in vivo* antitumor efficacy of our hydrogel system using the 4T1 breast cancer model. The results consistently demonstrated that HPC hydrogel exerted potent therapeutic effects, comparable to those observed in the B16 melanoma model (Figs. S14 and S15 in Supporting information). These findings highlight the potential of our hydrogel to achieve effective antitumor outcomes across different tumor types, underscoring its adaptability to heterogeneous TME.

In conclusion, we engineered a self-healing and injectable HPC hydrogel system to potentiate ferroptosis in malignant melanoma *via* CDT. Mechanistically, the $CuO_2$ nanoparticles within the hydrogel endogenously generated $H_2O_2$, effectively compensating for the endogenous $H_2O_2$ deficiency in TME. Moreover, the hydrogel system was capable of sustaining GSH depletion through dual $Cu^{2+}$/•OH-cycling mechanisms. The depletion of GSH led to the inactivation of GPX4, thereby triggering the ferroptotic cascade. The induced ferroptotic cascade exhibited remarkable anti-tumor efficacy and significantly curtailed metastatic dissemination. Our collective findings demonstrate that the self-healing hydrogel system possesses dynamic •OH-generating and GSH-scavenging capabilities. It shows significant potential as a viable platform for enhancing the susceptibility of melanoma cells to both CDT and ferroptosis induction, thus offering a novel therapeutic approach for melanoma treatment.

## Declaration of competing interest

The authors declare that they have no known competing financial interests or personal relationships that could have appeared to influence the work reported in this paper.

## CRediT authorship contribution statement

**Yongzhi Wu:** Writing – original draft, Software, Methodology, Investigation, Conceptualization. **Rong He:** Writing – original draft, Methodology, Investigation, Data curation. **Bowen Tan:** Methodology, Conceptualization. **Longjiang Li:** Writing – review & editing, Supervision, Funding acquisition, Conceptualization. **Jinfeng Liao:** Writing – review & editing, Supervision, Funding acquisition, Conceptualization.

## Acknowledgments

This work was financially supported by the National Natural Science Foundation of China (Nos. 32171354, 82372735). The authors thank BioRender.com (agreement Nos. VN280FZSDG, SZ280FZZZC, and PA280FZN1X) for providing the graphical tools used to create the schematic figures, including the graphical abstract, Fig. 1, and Fig. 4.

## Supplementary materials

Supplementary material associated with this article can be found, in the online version, at doi:10.1016/j.cclet.2025.111339.

## References

[1] G.V. Long, S.M. Swetter, A.M. Menzies, et al., Lancet 402 (2023) 485–502.
[2] L. Zhai, Y. Shi, Y. Yan, et al., Chin. Chem. Lett. 34 (2023) 108104.
[3] Y. Lin, X. Wang, S. He, et al., Acta Pharm. Sin. B 14 (2024) 854–868.
[4] I. Anestopoulos, S. Kyriakou, V. Tragkola, et al., Pharmacol. Ther. 240 (2022) 108301.
[5] L. Wang, S. He, R. Liu, et al., Acta Pharm. Sin. B 14 (2024) 2263–2280.
[6] P.B. Balakrishnan, D.K. Ledezma, J. Cano-Mejia, et al., Nano Res. 15 (2022) 2300–2314.
[7] S. Liang, Y. Liu, H. Zhu, et al., Exploration 4 (2024) 20230163.
[8] W. Yu, F. Jia, J. Fu, et al., ACS Nano 17 (2023) 15713–15723.
[9] X. Huang, T. He, X. Liang, et al., MedComm Oncol. 3 (2024) e67.
[10] D. Sheehan, K. Sheehan, J. Sheehan, J. Neurooncol. 153 (2021) 373–374.
[11] N.W. Nkune, H. Abrahamse, Int. J. Mol. Sci. 22 (2021) 12549.
[12] S. Sun, D. Wang, R. Yin, et al., Small 18 (2022) e2202558.
[13] P.C. Huang, E.J. Chaney, E. Aksamitiene, et al., Theranostics 11 (2021) 5620–5633.
[14] E.A. Thim, L.E. Kitelinger, F. Rivera-Escalera, et al., Theranostics 14 (2024) 1647–1661.
[15] C. Jia, Y. Guo, F.G. Wu, Small 18 (2022) e2103868.
[16] J. Tang, Y. Liu, Y. Xue, et al., Exploration 4 (2024) 20230127.
[17] Y. Zhou, S. Fan, L. Feng, et al., Adv. Mater. 33 (2021) e2104223.
[18] X. Chen, H. Yang, X. Song, et al., Chin. Chem. Lett. 34 (2023) 107753.
[19] P. Jin, X.D. Feng, C.S. Huang, et al., MedComm Oncol. 3 (2024) e70007.
[20] H. Hu, L. Yu, X. Qian, et al., Adv. Sci. 8 (2020) 2000494.
[21] L. Yuan, J. Tatineni, K.M. Mahoney, et al., Trends Immunol. 42 (2021) 209–227.
[22] C. Yin, Y. Tang, X. Li, et al., Small 14 (2018) e1703400.
[23] L.H. Fu, Y. Wan, C. Qi, et al., Adv. Mater. 33 (2021) e2006892.
[24] X. Chen, R. Kang, G. Kroemer, et al., Nat. Rev. Clin. Oncol. 18 (2021) 280–296.
[25] Q. Zhou, Y. Meng, D. Li, et al., Signal Transduct. Target. Ther. 9 (2024) 55.
[26] X. Han, F. Wang, J. Shen, et al., Adv. Mater. 36 (2024) e2306993.

[27] W. Yang, Q. Zhang, J. Zhou, et al., Biomacromolecules 25 (2024) 3432–3448.
[28] L. Kahlert, E.F. Bassiony, R.J. Cox, et al., Angew. Chem. Int. Ed. 59 (2020) 5816–5822.
[29] Y. Feng, Z. Zhang, W. Tang, et al., Exploration 3 (2023) 20220173.
[30] H. Xu, Z. Zhao, P. She, et al., J. Control. Release 375 (2024) 788–801.
[31] W. Zhang, Y. Shi, H. Li, et al., Carbohydr. Polym. 288 (2022) 119418.
[32] L.S. Lin, T. Huang, J. Song, et al., J. Am. Chem. Soc. 141 (2019) 9937–9945.
[33] F.X. Wang, Z.W. Zhang, F. Wang, et al., J. Colloid Interface Sci. 649 (2023) 384–393.
[34] Y. Bian, K. Zhao, T. Hu, et al., Adv. Sci. 11 (2024) e2403791.
[35] M. Zorrón, A.L. Cabrera, R. Sharma, et al., Adv. Sci. 11 (2024) e2403204.
[36] Y. Huang, L. Mu, X. Zhao, et al., ACS Nano 16 (2022) 13022–13036.
[37] Y. Peng, Q.Z. Liu, D. Xu, et al., Biochem. Pharmacol. 217 (2023) 115856.
[38] M.J. Woźniak-Budych, B. Maciejewska, Ł. Przysiecka, et al., J. Mol. Liquids 319 (2020) 114086.
[39] T. Liu, B. Xiao, F. Xiang, et al., Nat. Commun. 11 (2020) 2788.
[40] S. Naz, A. Gul, M. Zia, IET Nanobiotechnol 14 (2020) 1–13.
[41] T. Ameh, C.M. Sayes, Environ. Toxicol. Pharmacol. 71 (2019) 103220.
[42] I.C. Lee, J.W. Ko, S.H. Park, et al., Part. Fibre. Toxicol. 13 (2016) 56.